MATERIALS SCIENCE

# Disordered-nanoparticle–based etalon for ultrafast humidity-responsive colorimetric sensors and anti-counterfeiting displays

**Chunghwan Jung[1]†, Soo-Jung Kim[2]†, Jaehyuck Jang[1]†, Joo Hwan Ko[3], Doa Kim[2], Byoungsu Ko[4], Young Min Song[3], Sung-Hoon Hong[2]*, Junsuk Rho[1,4,5]***



**The development of real-time and sensitive humidity sensors is in great demand from smart home automation and modern public health. We hereby proposed an ultrafast and full-color colorimetric humidity sensor that consists of chitosan hydrogel sandwiched by a disordered metal nanoparticle layer and reflecting substrate. This hydrogel-based resonator changes its resonant frequency to external humidity conditions because the chitosan hydrogels are swollen under wet state and contracted under dry state. The response time of the sensor is ~$10^4$ faster than that of the conventional Fabry-Pérot design. The origins of fast gas permeation are membrane pores created by gaps between the metal nanoparticles. Such instantaneous and tunable response of a new hydrogel resonator is then exploited for colorimetric sensors, anti-counterfeiting applications, and high-resolution displays.**

## INTRODUCTION

The real-time detection of biological and chemical substances is an emerging topic with increasing interests in modern public health, environmental monitoring, and smart Internet of Things system. Accordingly, smart, intuitive, and small footprint gas sensors have attracted much attention with an increase in their market volume. There are various types of gas sensors that include conductometric semiconducting metal oxide sensor (*1*), mass-sensitive sensors (*2*), thermometric and calorimetric sensor (*3*), electrochemical sensor (*4*), and optical sensor (*5*). Among them, optical sensors have the promising features of instantaneous responses, state-of-art sensitivity, and high gas specificity (*5*). In particular, colorimetric sensors have attracted much attention because of high accessibility, straightforward detection, and visualization together with excellent sensitivity toward various external stimuli for practical applications.

The figure of merits of optical sensors is closely related to the type of stimuli-responsive materials that consists of an active medium in the sensor (*6*). The type of the active medium determines what kinds of external stimuli drive the dynamic changes of optical responses of the system. The representative examples include a plasmonic system incorporated with metal hydrides varied by heat (*7*) and monoatomic gases (*8*); planar optical system with liquid crystal for detection of heat (*9*), pressure (*9*), or toxic gases (*10*); and Mie cavities composed of nanoporous titania for humidity sensing (*11*, *12*). Transparent hydrogels or polymers are widely selected as the active medium because they can absorb chemical substances such as moisture (*13*, *14*) or volatile gas (*15*, *16*) from their surroundings. When absorbing the substances, the hydrogels are swollen; such changes in physical geometries lead to the change of its optical properties as well. For precise detection, the optical signals from these changes are amplified using the carefully designed optical cavity (*17*). The typical geometries of a cavity include a multilayer interferometer such as the Bragg structure (*6*, *14*, *18*), hydrogel film on a reflective surface (*16*, *19*–*22*), and Fabry-Pérot etalon (*23*–*26*). The Bragg structure composed of alternating layers with different refractive indices allows broad bandwidth tuning; however, the large thickness of the whole device results in a slow response time of more than a dozen seconds. The hydrogel film on a reflective surface exhibits a rapid response time of hundreds of milliseconds because the hydrogel layer is exposed to the environment. The resonance of the film on a mirror relies on Fresnel reflection, thus resulting in low quality factor ($Q$ factor) and poor wavelength selectivity. In general, the resonator with a high $Q$ factor is preferred because of the superior sensitivity of the sensor, i.e., notable wavelength shift, optical absorption change, and color difference. Accordingly, Fabry-Pérot etalon, a hydrogel layer sandwiched by two parallel reflecting surfaces, has been proposed; this resonator allows the light at a resonant wavelength to pass through, therefore exhibiting high–$Q$ factor resonance (*23*, *27*). However, the top reflecting layers hinder the gas molecules from absorbing into the hydrogel layer so that the response time to reach the equilibrium state is rather slow, up to approximately an hour (*23*). Therefore, the development of a fast responsive and high–$Q$ factor hydrogel resonator is in great demand.

In this study, we propose an ultrafast colorimetric sensor platform using a tunable Fabry-Pérot–like resonator. The tunable Fabry-Pérot–like resonator is composed of a gas-responsive medium in between the top disordered metal nanoparticle (MNP) layer and bottom metallic mirror. We chose a chitosan hydrogel film as one example so that the fabricated resonator has a tunable resonant frequency with respect to external humidity conditions. Application of the MNP layer as an upper metal markedly reduces the response time of the sensor (<140 ms) because the membrane pores created by the gap between MNP nanoclusters increase gas permeability. An interparticle distance of MNPs, a key factor to determine the responsive time, is manipulated by the exchange of the ligand attached to MNPs. Moreover, the ligand exchange results in the disorders of MNPs,

[1]Department of Chemical Engineering, Pohang University of Science and Technology (POSTECH), Pohang 37673, Republic of Korea. [2]ICT Materials and Components Research Laboratory, Electronics and Telecommunications Research Institute (ETRI), Daejeon 34129, Republic of Korea. [3]School of Electrical Engineering and Computer Science, Gwangju Institute of Science and Technology (GIST), Gwangju 61005, Republic of Korea. [4]Department of Mechanical Engineering, Pohang University of Science and Technology (POSTECH), Pohang 37673, Republic of Korea. [5]POSCO-POSTECH-RIST Convergence Research Center for Flat Optics and Metaphotonics, Pohang 37673, Republic of Korea.
*Corresponding author. Email: shong@etri.re.kr (S.-H.H.); jsrho@postech.ac.kr (J.R.)
†These authors contributed equally to this work.

i.e., disordered NP system that recently gained a great amount of interest (*28*–*32*). The induced disorders become the origin of the highly absorbing dielectric optical properties of the MNP layer, which enables more vivid and marked coloration in reflection compared to structural coloration based on conventional Fabry-Pérot resonators. The increased gas permeability and highly absorbing dielectric properties lead to the instantaneous resonance shifts upon the change of the surroundings, thus displaying the instantaneous color change and the value of the current relative humidity (RH) very quickly (text S1). As an application, we devised anti-counterfeiting quick response (QR) displays that are visible normally but hidden in a certain range of RH. In addition, we demonstrate a full-color large-scale display with unit pixel sizes of 10, 5, and 2 μm corresponding to 2540 pixels per inch (PPI), 5080 PPI, and 12,700 PPI, respectively.

## RESULTS AND DISCUSSION

### Geometry of MNHM structure

The MNP-hydrogel-mirror (MNHM) structure is prepared by substituting plasmonic NPs for an upper metal reflector in a conventional Fabry-Pérot resonator (Fig. 1A). In detail, the MNHM resonator was composed of an aluminum (Al) reflector, chitosan film, and silver (Ag) NP layer, and the details of fabrication processes are described in note S1. The morphology of the upper NP layer relies on the types of surface ligands: oleylamine (OLA) and thiocyanate (SCN) (*33*, *34*). The synthesized 10-nm-diameter Ag NPs are surrounded by OLA ligands (AgNPs-OLA) on their surfaces. The long alkyl chain of OLA restricts the interaction between Ag NPs and can form a continuous thin film while maintaining the distance between Ag NPs. In contrast, manipulating the surface ligands of the NPs to replace them with the short monomolecular ligand SCN shortens the interparticle separation, and Ag NPs are aggregated with each other. Through the ligand exchange from OLA to SCN ligands, the randomly distributed spherical nanoclusters composed of SCN-capped Ag NPs (AgNPs-SCN) have been chemically created and formed a porous layer with space available for gas penetration (Fig. 1B and note S2). The chitosan hydrogel, which was adopted as an active medium, has a unique property that can swell reversibly and rapidly by absorbing the surrounding water at almost 1000 weight % (wt %) of its dried weight due to the strong hydrogen bonding between the chitosan polymer and water molecules (Fig. 1C) (*35*, *36*). As moisture absorbs and expands the hydrogel layer, the refractive index gradually decreases, and the thickness gradually increases along with the external humidity (note S3). The initial thickness of the chitosan layer is determined by the concentration of chitosan solution and the speed of spin coating (note S4). Every experiment, except note S4, used a hydrogel layer that is spin-coated with 2% chitosan solution at 2500 rpm.

### Optical response of MNHM structure

MNHM etalon using AgNPs-SCN (MNHM-SCN) has a tunable resonant frequency dependent on the thickness and the refractive index of hydrogel layers. Unlike the conventional Fabry-Pérot film, the reflection spectrum of the MNHM-SCN shows a single peak and vivid color similar to the transmission spectrum of Fabry-Pérot resonator (Fig. 2A). The underlying physics closely relate to MNPs on top that act like a highly absorbing dielectric layer (*34*). Moreover, the randomly dispersed (disordered) subwavelength MNPs are known to have material-independent broadband absorption (*28*–*31*, *37*), thus enabling sharper reflection peaks and more vivid colors than metal-insulator-metal cavities (*34*). For the detailed analysis of MNHM etalon, we calculated the effective refractive index of AgNPs-SCN slab (text S2) and derived the overall reflection coefficient of the etalon based on scattering matrix models (text S3).

As a colorimetric sensor application, an MNHM-SCN resonator with the hydrogel layer thickness of 150 nm at RH 60% is prepared. The reflection spectra of the MNHM-SCN resonator are measured under various RH conditions by using a specially designed chamber and spectrometer (Fig. 2A, Materials and Methods, and note S5). An increase in RH induces a redshift of resonant wavelength; such peak shift of single and sharp resonance in visible light results in vivid coloration (insets in Fig. 2A). Color swatches from both the finite-difference time-domain (FDTD) method and the captured one are identical; the color gamut of single sensor devices covers 90% of the standard red, green, and blue (sRGB) gamut in CIE 1931 color space (Fig. 2B). The wide coverage in color space originates from the hydrogel's capacity to store waters and expand its volumes. In our experiments, the volume of hydrogel is expanded up to 2.5 times, which is matched to the one in the literature (*38*). In particular, the swelling at around RH 80% becomes radical, thus leading to the rapid change of colors over RH 80% (Fig. 2C). The resonance peak shifts from 400 to 532 nm in an increase in RH from 80 to 90% only. We expected the larger range of peak shifts up to RH 100%, although such high-RH conditions are prohibited because of the RH limit of the measurement setup. In addition, the effect of the incident angle of light in the MNHM-SCN was calculated (note S6). As the incident angle increases up to 30°, the reflection peak is blueshifted in both transverse electric (TE) and transverse magnetic (TM) modes.

The effective refractive index of the AgNPs-SCN slab is retrieved using a well-established S-parameter retrieval technique (*39*, *40*). The effective parameters are greatly affected by geometrical parameters such as size and dispersion of the NPs; for instance, one can suppress the contribution of material properties to absorption spectra by randomly arranging metallic NPs (*28*). Therefore, we realistically model the AgNPs-SCN slab based on measured scanning electron microscope (SEM) images and atomic force microscope (AFM) data (Fig. 2D and note S2). The position and the radius ranged from 10 to 35 nm are set as the random variables, and those variables are changed each iteration. The iteration is executed 100 times; the retrieved S parameters from all executions are used to calculate the arithmetic mean that defined the effective S parameters in this context. The calculated effective refractive indices display abnormal dispersion so that both real $\Re(n_{NP})$ and imaginary parts $\Im(n_{NP})$ increase with an increase in wavelength (Fig. 2E). This underpins our claims that the AgNPs-SCN acts as a highly absorbing dielectric layer unlike a metallic slab. It is notable that in-plane deformation by hydrogel swelling can be ignored, and the AgNPs-SCN structure and effective refractive indices are unchanging over the humidity because the thickness of the hydrogel layer is very small compared to its width.

The resonance features of MNHM etalon are then analyzed using a scattering matrix model that considers the lossy dielectric layer (text S3). The reflection coefficient $r_{15}$ can be calculated as follows

$$r_{15} = r_{12} + \frac{t_{12}t_{21}P_{NP}^2}{1 - r_{21}r_{23}P_{NP}^2} \left( r_{23} + t_{23}t_{32}P_H^2 \left( 1 - P_H^2 \left( r_{32} + \frac{r_{21}t_{32}t_{23}P_{NP}^2}{1 - r_{21}r_{23}P_{NP}^2} \right) \right)^{-1} \right) \quad (1)$$

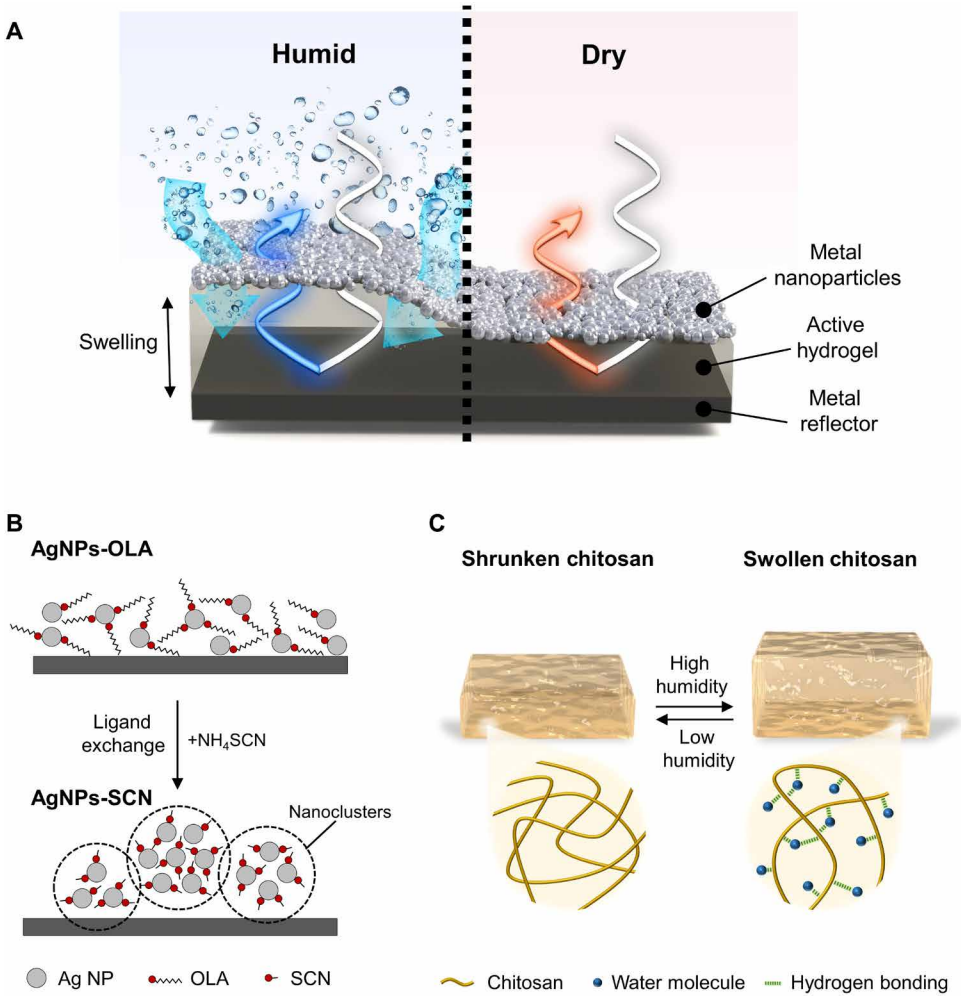


**Fig. 1. Graphical illustration of MNHM etalon and its ingredients.** (**A**) Schematics of MNHM etalon under the humid and dry state of the surrounding. (**B**) Ligand exchange of AgNPs-OLA transformed to AgNPs-SCN. The aggregated nanoclusters form membrane pores that aid the penetration of gas into the hydrogel layer. Gray circle, Ag NP; dot with zigzag tail, OLA ligand; dot with straight tail, SCN ligand. (**C**) Swelling/contraction of chitosan hydrogel under the change of humidity condition. Yellow line, chitosan network; blue dot, water molecule; green dashed line, hydrogen bonding between the chitosan network and water molecules.

where $P_{NP} = \exp(-(\frac{\alpha_{NP}}{2} + \hat{i}\ \Re(n_{NP})\, k_0)\, d_{NP})$ and $P_H = \exp(-\hat{i}\, n_H\, k_0\, d_H)$; $r_{ij}$ and $t_{ij}$ are the reflection and transmission coefficients of light passing through the $i$th to $j$th layer; $\alpha_{NP}$ is the attenuation factor of the NP layer; $n_{NP}$ and $n_H$ are the real part of the refractive index of the NP and hydrogel layer; $d_{NP}$ and $d_H$ are the thickness of the NP layer and hydrogel layer; and $k_0$ is the wave vector of incident light. Here, $P_{NP}$ and $P_H$ are the terms that consider attenuation and phase change that occur during the propagation. This propagation factor contributes to the resonant features of MNHM-SCN etalon that are sensitive to structural and optical modification in an insulating layer. The values from the analytical approach are in great agreement with the measured data and FDTD simulation results (Fig. 2A), which implies that our scattering matrix models are valid.

The electric field distributions of the MNHM-SCN etalon at RH 90% are represented at the resonant peak and dip (Fig. 2F). The electric field at the peak is localized in the dielectric layer, thus creating the resonant mode in the cavity. However, the electric field at the dip is formed adjacent to the AgNPs-SCN layer, which indicates that absorption of electromagnetic energy in the NP layer is dominant. The same tendency is observed in the retrieved effective medium (note S7). Another interesting thing is that the disordered NPs are hardly interrupting the wavefront of the plane wave passing through (note S8).

In short, our MNHM-SCN resonator has a tunable resonant frequency with respect to external humidity conditions. The resonance shifts upon the change of the surroundings lead to the instantaneous color change, thus displaying the value of the current RH very quickly, i.e., colorimetric humidity sensor.

## Response time of MNHM structure

The response time of our MNHM etalon is much faster than the one of the film-type etalon. This is because membrane pores, related to an interparticle distance of nanoclusters, could allow gas molecules to penetrate the MNP layer when the pore size is much bigger than the gas molecule but smaller than the mean free path of the gas molecule; that is called the Knudsen diffusion (*41*). However, when the pore is too large, the MNP layer may lose its interesting absorbing feature vital to form strong Fabry-Pérot resonances in the cavity.

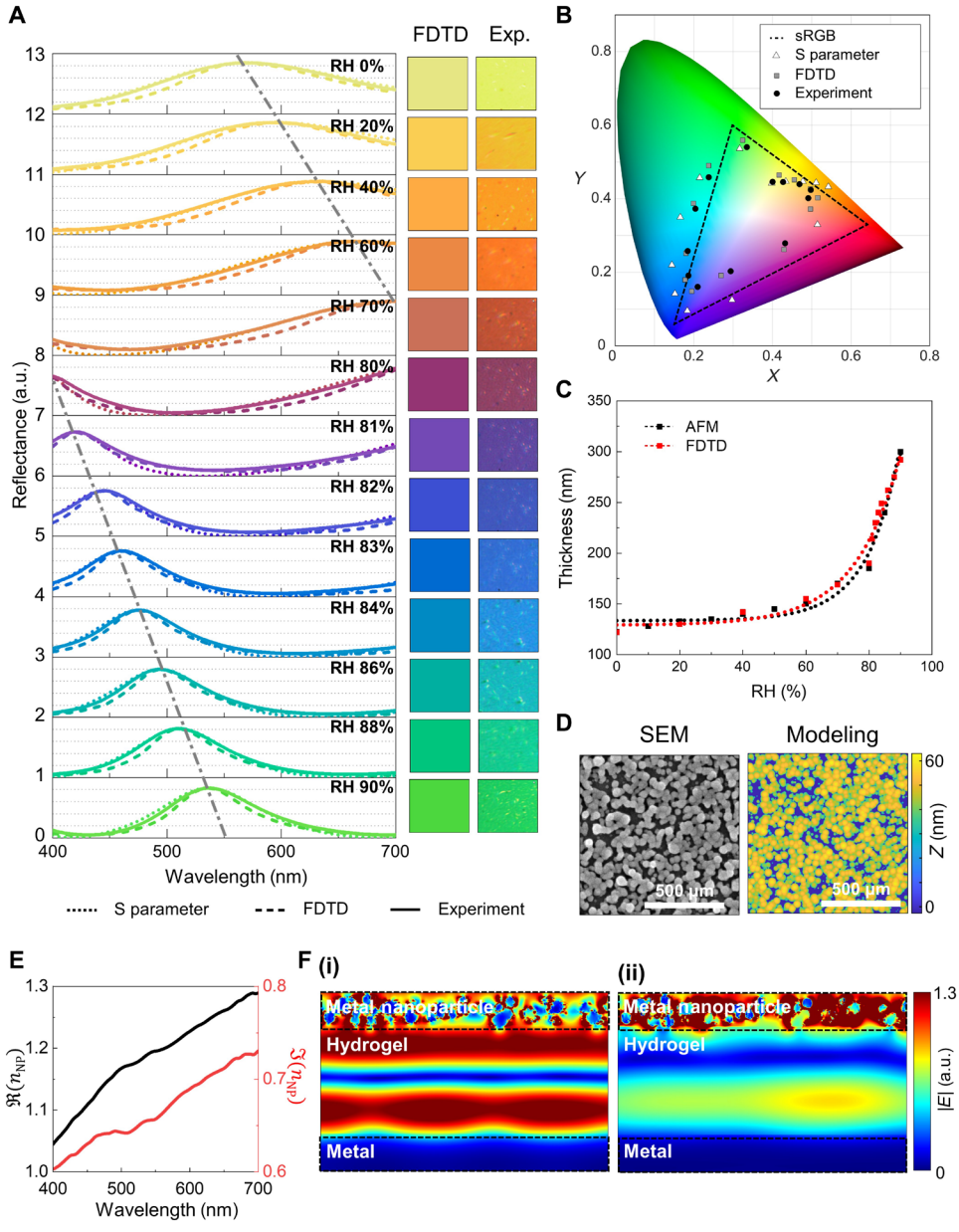


**Fig. 2. Optical responses of MNHM etalon.** (**A**) Reflection spectra of MNHM-SCN etalon at RH ranged from 0 to 90%. Dotted line, spectra retrieved from S parameters; dashed line, spectra calculated by FDTD method; solid line, measured spectra. Insets represent calculated and measured color swatches at the same range of RH. a.u., arbitrary units. (**B**) CIE 1931 color space of the *XY* values converted from the reflection spectra. (**C**) The change of thickness of the chitosan layer according to RH that is measured and calculated by AFM and FDTD. (**D**) SEM and modeled images of AgNPs-SCN slab. The color bar in the modeled one indicates depth information *z* at each pixel. (**E**) Effective refractive indices retrieved from S-parameter analysis. Black, real; red, imaginary. The dashed triangle shows the sRGB space. Triangle, S parameters; square, FDTD; circle, measurement. (**F**) Normalized electric field distribution of MNHM-SCN etalon (i) at the peak of the reflectance, 532 nm, and (ii) at the dip of the reflectance, 676 nm, both under RH 90%.

By the ligand exchange process, the balanced construction for both optical and temporal properties has been achieved.

For the comparison of response/recovery times of sensors, we prepared the following four devices: (i) hydrogel on a mirror (HM), (ii) (AgNPs-OLA)–hydrogel–mirror (MNHM-OLA), (iii) MNHM-SCN, and (iv) (Ag film)–hydrogel–mirror (MHM). The response/recovery time is defined as the amount of time required to reach 90% intensity of the equilibrium state ($T_{90}$). The measured response times of HM, MNHM-OLA, MNHM-SCN, and MHM device are 119, 304, 141, and 3,800,000 ms (Fig. 3A). The recovery times are 107, 394, 140, and 3,000,000 ms, respectively (Fig. 3B). Our device, i.e., MNHM, has a very rapid response time almost close to the case of the hydrogel layer exposed to the surroundings and shows a great enhancement (~$10^4$) in reaction speed compared to the conventional film-type etalon. In addition, it is notable that the time delay could be reduced by the optimization of the upper metal layer. For example,

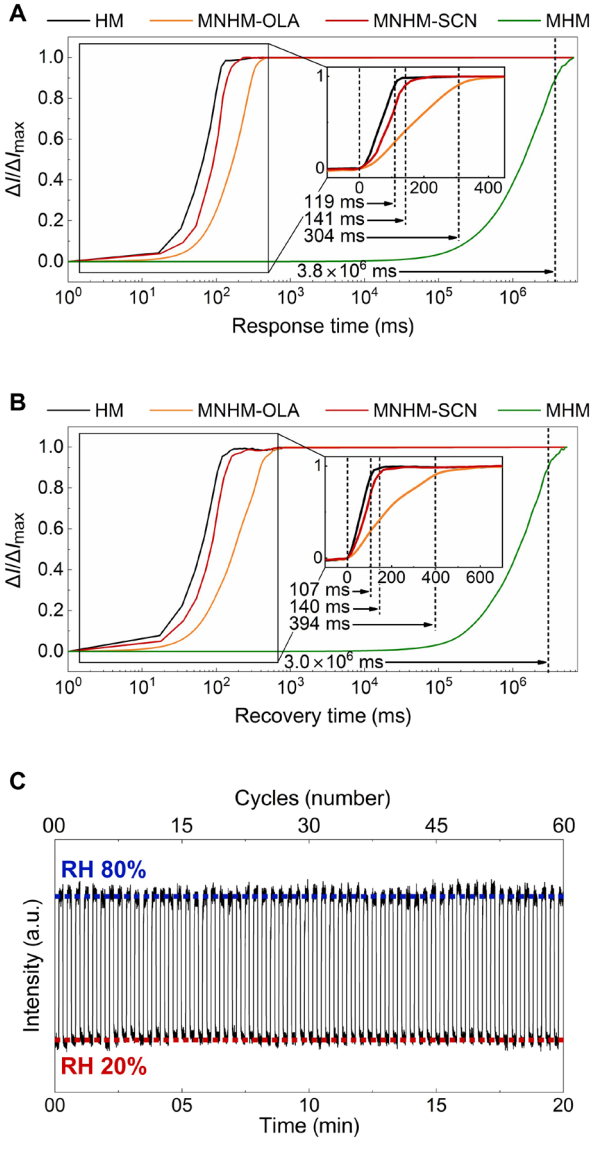


**Fig. 3. Measurement of response/recovery time and repeatability of MNHM sensor.** Comparison of (**A**) response time and (**B**) recovery time of various resonators. The ratio of real-time intensity $\Delta I$ to the intensity in the equilibrium state $\Delta I_{max}$ at the resonant wavelength was measured. Black, HM; orange, MNHM-OLA; red, MNHM-SCN; green, MHM. (**C**) The repeatability test of MNHM-SCN was conducted by measuring real-time intensity under two repeatedly changed states of RH 20 and 80%. Each state was maintained for 10 s and repeated 60 times. Concentration of the chitosan solution, 2%. Spin-coating speed, 2500 rpm.

although MNHM-SCN has the same amount of AgNPs as MNHM-OLA, its response time was improved by as much as 160 ms due to the porous structure formed by ligand exchange.

Repeatability test of our sensor was conducted by repeating two states of RH 20 and 80% periodically. Each state was maintained for 10 s and repeated 60 times. As chitosan hydrogels are capable of repeating absorption and release of water, our sensor proves its repeatability without any degradation after the test (Fig. 3C). In particular, chemically linked AgNPs-SCN sustains optical and chemical stability when exposed to high temperature (85°C) and humidity (RH 85%) for a long time (24 hours), demonstrating the reliability of the proposed MNHM sensor (note S9). The MNHM-SCN device did not oxidize and operated normally even after 6 months of production.

## Application toward security label and high-resolution display

Vivid and humidity-responsive structural colors from MNHM-SCN etalon enable state-of-art security labeling for anti-counterfeits (*42*). Here, we present a three-dimensional (3D) QR code to which a show/hide function is added by introducing humidity-responsive color pixels into the security code; this 3D code can go beyond the existing 2D QR code that records information only with two contrasted unit pixels, e.g., black and white, in a 2D plane.

As examples for the 3D QR code, we prepared the two QR codes that are colored by three kinds of unit pixels (Fig. 4A). Pixels 1 and 3 are humidity-invariant pixels made up of MNP-$SiO_2$-reflector with different insulator thickness. On the other hand, pixel 2 is a humidity-responsive pixel made up of MNHM-SCN. To reveal/conceal the printed images in a certain range of RH, we designed pixels 1 and 3 to have a similar reflection spectrum to that of pixel 2 under low (RH 40%) and high (RH 85%) humidity (Fig. 4B). The first QR code consists of pixels 1 and 2; the background that remained unchanged with respect to external humidity is colored by fixed orange color, i.e., pixel 1, and the rest by pixel 2 of which color is changed from orange at low RH to green at high RH (top images in Fig. 4C). Because the color of pixels 1 and 2 is very similar to each other, the QR code becomes bad to be scanned at a range of low RH. Under humidity higher than 80%, the code becomes fairly readable. The second QR code is constructed of pixels 2 and 3 in a similar fashion. In this case, the background is colored by humidity-responsive pixel 2, and the rest is colored by fixed blue color, i.e., pixel 3. This second code is readable for most cases but becomes indistinguishable at RH ~85%. A little bit of color nonuniformity of the security labels depends on fabrication error—i.e., edge-bead effect, incomplete liftoff, and thickness deviation at the sidewall—and could be improved by optimization of the fabrication process. The proposed 3D security codes can be more complex with a larger number of unit pixels considered in the design.

It is important to determine how finite the size of MNHM structure is while maintaining the vivid color expression for the application toward new-generation color filtering and display. Here, we successfully fabricated the pixelated MNHM-SCN structures having five different heights with a pixel pitch of 10 μm (2540 PPI), 5 μm (5080 PPI), and 2 μm (12,700 PPI) (Fig. 5A). A multistep $SiO_2$ layer with five different heights was added on the bottom reflector of the MNHM-SCN structure to make different colors. The step height is designed to be 60 nm to express orange, red, blue, green, and yellow colors at RH 0%. Despite the resolution of more than 10,000 PPI, the MNHM-SCN structure showed a uniform color, consistent with the intended design. In addition, these pixels rapidly switch their colors in response to the change of external humidity (Fig. 5B), thus highlighting the essence of this study. The colors from each pixel change markedly with humidity, affecting the display color as seen with the naked eye. This color change according to humidity was plotted on the CIE 1931 diagram (note S10).

In summary, we introduced disordered NP-based etalon structure for fast change of optical response, i.e., spectrum, and its application toward colorimetric sensors. The proposed structure accomplishes vivid full-color changes and ultrafast responses (~0.1 s) because the

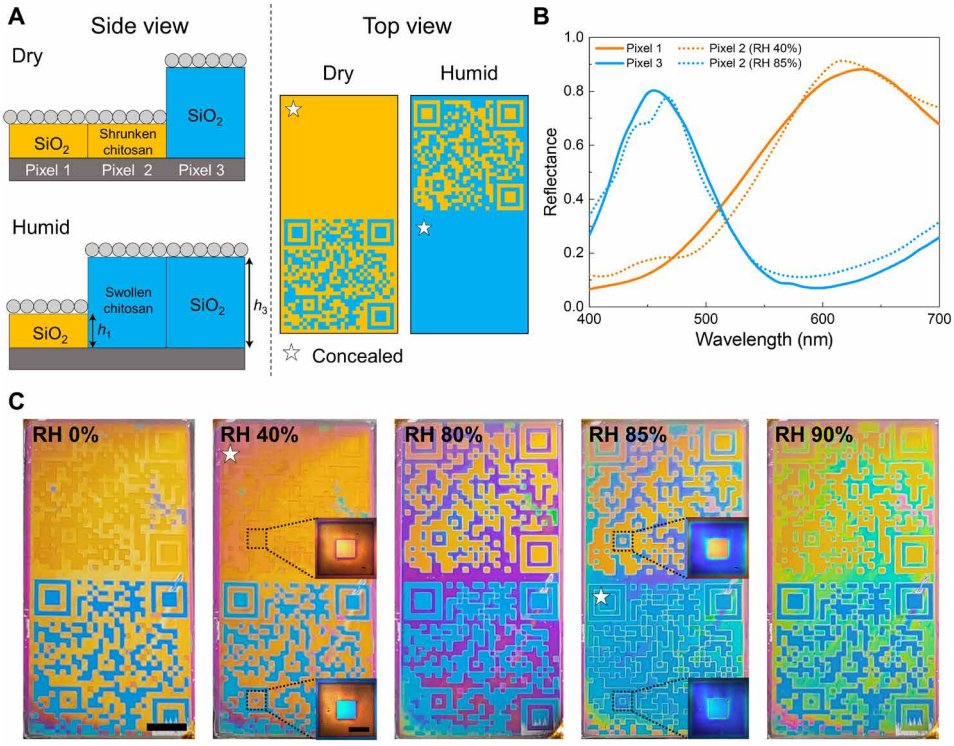


**Fig. 4. Humidity-responsive security labels.** (**A**) Side and top views of two QR codes linked to Pohang University of Science and Technology and Electronics and Telecommunications Research Institute webpages. Two QR codes are colored by three types of unit pixels: a humidity-invariant pixel made up of MNP-$SiO_2$-reflector with insulator thickness $h_1 = 180$ nm (pixel 1) and thickness $h_3 = 280$ nm (pixel 3) and a humidity-responsive one made up of MNHM-SCN (pixel 2). (**B**) The reflection spectrum of the three pixels. Orange solid line, pixel 1; blue solid line, pixel 3. Orange dashed line, pixel 2 under RH 40%; blue dashed line, pixel 2 under RH 85%. (**C**) Optical images of two QR codes under varied RH conditions. Upper QR codes consist of pixels 1 and 2, and lower ones consist of pixels 2 and 3. Scale bar, 2.5 mm. Insets: Boundary of two different pixels with a scale bar of 400 μm.

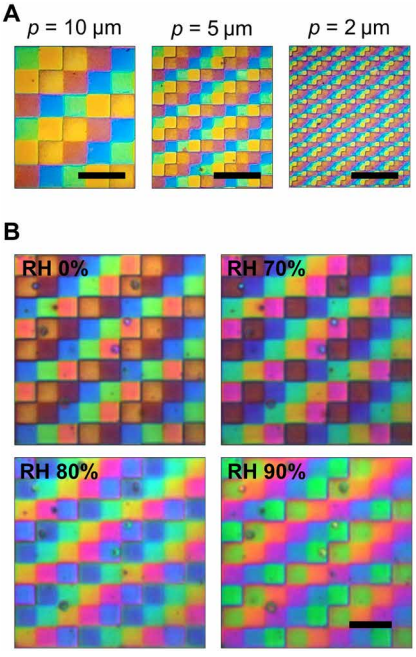


**Fig. 5. High-resolution display using MNHM-SCN structures.** (**A**) Pixelated MNHM-**SCN** etalon with a pixel size of 10 μm (2540 PPI), 5 μm (5080 PPI), and 2 μm (12,700 PPI). (**B**) Pixelated MNHM etalon (2540 PPI) under RH 0, 70, 80, and 90%. Scale bars, 20 μm.

disordered MNPs form membrane pores smaller than the mean free path of penetrating gas, known as the Knudsen diffusion. The distance between adjacent NPs acting as pores is an important factor to determine the response time of the device. Because the interdistance is determined by the type of ligands attached to the MNP, we compare three types of samples in terms of temporal and spectral features: AgNPs-OLA, AgNPs-SCN, and metallic film as the top layer on hydrogel–(bottom reflector)–substrate. Optical characteristics of the disordered NP-based etalon, especially with SCN ligands, are measured and analyzed by FDTD simulation and analytic equation using S-parameter retrieval method. The analysis proves that the disorders induced by the ligand exchange result in highly absorbing dielectric properties of AgNPs-SCN, which becomes the origin of rich coloration in the proposed etalon structure. In addition, we demonstrated 3D QR codes and pixelized displays that dynamically changed in response to external humidity, thus highlighting the potential toward colorimetric sensor and anti-counterfeiting display. More notably, we expect that such MNP–(gas-responsive layer)–mirror concept could also be expanded to optical sensors to detect various gases and water vapor. For instance, incorporation of our concept into catalytic metal (*43*, *44*), block copolymer photonic crystals (*18*), or several hydrogels (*19*, *24*, *45*) may enable ultrafast and colorimetric sensing of monoatomic gases such as hydrogen and oxygen, volatile organic compounds, and toxic gases such as hydrogen sulfide and nitrogen oxide. We believe that our MNHM structure could be applied to real-time gas sensing, security labeling, and smart display.

## MATERIALS AND METHODS

### Materials

Medium–molecular weight chitosan with a deacetylation degree of 75 to 85% and molecular weight of 190,000 to 310,000 Da, acetic acid (ACS reagent, ≥99.7%), and ammonium hydroxide ($NH_4OH$) solution [puriss, 30 to 33% ammonia in deionized (DI) water] were purchased from Sigma-Aldrich and used without further purification. Isopropanol and acetone were purchased from Duksan General Science and used without further purification. A high-purity (99.9%) Al was obtained from E-Tek. Glass was diced to a size of 20 mm by 20 mm and used as a substrate for preparing chitosan coatings.

### Device fabrication

For (i) substrate preparation, substrates were sonicated and cleaned with DI water, acetone, and isopropanol and dried using a nitrogen gun. A 100-nm-thick Al reflector was deposited in an electron-beam (e-beam) evaporation. For the (ii) formation of chitosan layer, chitosan solution (concentration, 2.0 wt %) was prepared by dissolving the chitosan powder in 50-ml DI water that contained 2.0 wt % acetic acid. The solution was stirred under heating overnight at 2000 rpm and 65°C and then centrifuged at 4500 rpm and 25°C for 3 hours. After centrifugation, the solution was filtered with 0.8-μm (cellulose acetate, 25 mm, Hyundai Micro) and 0.45-μm (nylon, 25 mm, Hyundai Micro) syringe filters sequentially. To obtain thin polymer films, chitosan solution was spin-coated onto Al-deposited glass for 5 s at 1000 rpm and then for 1 min at 2500 rpm. The chitosan films were dried at ambient atmosphere for 2 hours and then deprotonated by immersion in 3.0 wt % ammonia solution for 10 min, followed by thorough rinsing with distilled water. For the (iii) manipulation of surface ligands for closely coupled AgNPs-SCN layer (ligand exchange process), a dispersion of as-synthesized 10-nm-diameter Ag NPs in octane was prepared, and Ag NPs are surrounded by OLA organic ligands on their surfaces. A colloidal dispersion of Ag NPs filtered through a 0.45-μm syringe filter (polytetrafluoroethylene, 25 mm, Whatman) was uniformly spin-coated onto the chitosan layer at 3000 rpm. Then, the heat treatment was carried out at 100°C for 1 min to stabilize the NP layer. To manipulate the surface ligands of Ag NP and form the closely connected Ag NPs, the solid ligand exchange was performed. The Ag NP–coated thin film was immersed in an isopropyl alcohol (IPA) solution containing 1% ammonium thiocyanate ($NH_4SCN$) alternative ligands for 1 min to induce ligand exchange from the original OLA to SCN ligands. The treated samples were transferred to a pure IPA bath and washed to remove nonspecifically bound ligands.

### Measurement process

Thickness and surface morphology of spin-coated chitosan films and Ag NPs on glass wafers were measured in a certain RH by AFM (Park Systems, XE7). The measurements were performed at room temperature (20° ± 2°C). The Ag NP films on silicon wafer were evaluated using an x-ray diffractometer (D/Max-2500, Rigaku, Japan). The x-ray diffraction angles were measured from 10° to 90°, and the transmittance of films was evaluated using an ultraviolet-visible (UV-vis) near-infrared spectrometer (Lambda 750, PerkinElmer, USA) with the wavelength from 250 to 1000 nm. A UV-vis spectrophotometer (UV-2600Plus, Shimadzu, Japan) was used to measure the reflectance. The chitosan was spin-coated at 2500 rpm. The reflectance of samples of various RH of chitosan-based devices was measured with a specially designed humidity chamber to control the RH. To change the RH, the humid gas that comes through DI water was supplied in the chamber. The measurements were conducted at room temperature (20° ± 2°C).

### Fabrication of color security QR code and high-resolution display

The color security code with multi–confidential information stored was fabricated through a photolithography process base. The reflective Al layer was deposited via e-beam evaporation onto a cleaned silicon wafer. Then, 500-nm-thick $SiO_2$ layers were deposited at 200°C by using plasma-enhanced chemical vapor deposition (PECVD). The i-line stepper–based lithography process and dry etching were sequentially performed so that the 3D QR code patterns representing the Electronics and Telecommunications Research Institute research center information and Rho's laboratory information have different $SiO_2$ thicknesses. First, the photoresist (PR) protection layer of background area (excluding QR code pattern) was created using a 1.03-μm-thick PFi38A (Sumitomo) PR. Then, $SiO_2$ layer was selectively etched to 500 nm through a low-pressure high-density plasma etch process (etch rate, 5 Å/s). Similarly, PR patterns in both QR codes were formed, and $SiO_2$ layers with thicknesses of 280 and 180 nm were fabricated through an etching process, respectively. To create a chitosan layer only on the surface of the background region through a liftoff process, PR blocking layer was formed to cover all the QR patterns, and a 140-nm-thick chitosan layer was deposited as described above. After the liftoff process with acetone and cleaning, AgNPs-SCN thin layer was coated in the manner mentioned above to produce color. Similarly, the display device was designed to have five different heights of $SiO_2$ layer on the bottom reflector in 2 μm–by–2 μm, 5 μm–by–5 μm, and 10 μm–by–10 μm pixels. $SiO_2$ layers (235 nm thick) were first deposited by PECVD. The multistep $SiO_2$ layer was fabricated through repeating the photolithography for PR blocking layer and etching process four times (etching depth, 60 nm). Last, chitosan and AgNPs-SCN layers are deposited uniformly on the fabricated sample.

### Simulation

Reflectance spectra were generated using the FDTD method simulation using a commercial software, Lumerical FDTD solution. The Ag NPs are randomly scattered in 500 μm by 500 μm. The radius and position of the NPs were randomly distributed. Every physical parameter of the layer was chosen to match the SEM image. The FDTD simulations were repeated 10 times with different seeds to reflect the randomness of the layer. S-parameter (S11, S12, S21, and S22) calculation to get the effective refractive index of the NP layer proceeded using the embed function in Lumerical FDTD solution and retried 100 times with different seeds to get to reflect the randomness of the layer. The effective material properties were extracted using a MATLAB code developed by the authors. The refractive index of the $SiO_2$ substrate was set to 1.430. Chromaticity simulations were executed using the color-related MATLAB toolbox named OptProp. For color conversions, the CIE 1931 observer function with D50 was selected.

## SUPPLEMENTARY MATERIALS

Supplementary material for this article is available at https://science.org/doi/10.1126/sciadv.abm8598

## REFERENCES AND NOTES

1. C. Wang, L. Yin, L. Zhang, D. Xiang, R. Gao, Metal oxide gas sensors: Sensitivity and influencing factors. *Sensors* **10**, 2088–2106 (2010).

2. P. Gründler, *Chemical Sensors: An Introduction for Scientists and Engineers* (Springer Berlin Heidelberg, 2007); http://link.springer.com/10.1007/978-3-540-45743-5.
3. X. Liu, S. Cheng, H. Liu, S. Hu, D. Zhang, H. Ning, A survey on gas sensing technology. *Sensors* **12**, 9635–9665 (2012).
4. M. Khan, M. Rao, Q. Li, Recent advances in electrochemical sensors for detecting toxic gases: $NO_2$, $SO_2$ and $H_2S$. *Sensors* **19**, 905 (2019).
5. J. Hodgkinson, R. P. Tatam, Optical gas sensing: A review. *Meas. Sci. Technol.* **24**, 012004 (2013).
6. H. Megahd, P. Lova, D. Comoretto, Universal design rules for flory–Huggins polymer photonic vapor sensors. *Adv. Funct. Mater.* **31**, 2009626 (2021).
7. F. Shu, F. Yu, R. Peng, Y. Zhu, B. Xiong, R. Fan, Z. Wang, Y. Liu, M. Wang, Dynamic plasmonic color generation based on phase transition of vanadium dioxide. *Adv. Opt. Mater.* **6**, 1700939 (2018).
8. F. Neubrech, X. Duan, N. Liu, Dynamic plasmonic color generation enabled by functional materials. *Sci. Adv.* **6**, eabc2709 (2020).
9. I. Kim, M. A. Ansari, M. Q. Mehmood, W. Kim, J. Jang, M. Zubair, Y. Kim, J. Rho, Stimuli-responsive dynamic metaholographic displays with designer liquid crystal modulators. *Adv. Mater.* **32**, 2004664 (2020).
10. I. Kim, W.-S. Kim, K. Kim, M. A. Ansari, M. Q. Mehmood, T. Badloe, Y. Kim, J. Gwak, H. Lee, Y.-K. Kim, J. Rho, Holographic metasurface gas sensors for instantaneous visual alarms. *Sci. Adv.* **7**, eabe9943 (2021).
11. S. Mohd-Noor, H. Jang, K. Baek, Y. R. Pei, A. M. Alam, Y. H. Kim, I. S. Kim, J. H. Choy, J. K. Hyun, Ultrafast humidity-responsive structural colors from disordered nanoporous titania microspheres. *J. Mater. Chem. A* **7**, 10561–10571 (2019).
12. N. Jarulertwathana, S. Mohd-Noor, J. K. Hyun, Mesoporous solid and yolk–shell titania microspheres as touchless colorimetric sensors with high responsivity and ultrashort response times. *ACS Appl. Mater. Interfaces* **13**, 44786–44796 (2021).
13. J. Fu, F. Yang, Z. Guo, The chitosan hydrogels: From structure to function. *New J. Chem.* **42**, 17162–17180 (2018).
14. H. S. Kang, S. W. Han, C. Park, S. W. Lee, H. Eoh, J. Baek, D.-G. Shin, T. H. Park, J. Huh, H. Lee, D.-E. Kim, D. Y. Ryu, E. L. Thomas, W.-G. Koh, C. Park, 3D touchless multiorder reflection structural color sensing display. *Sci. Adv.* **6**, eabb5769 (2020).
15. A. Y. Mironenko, A. A. Sergeev, A. E. Nazirov, E. B. Modin, S. S. Voznesenskiy, S. Y. Bratskaya, H2S optical waveguide gas sensors based on chitosan/Au and chitosan/Ag nanocomposites. *Sens. Actuators B* **225**, 348–353 (2016).
16. Y. J. Yoo, W. Kim, J. H. Ko, Y. J. Kim, Y. Lee, S. G. Stanciu, J. Lee, S. Kim, J. Oh, Y. M. Song, Large-area virus coated ultrathin colorimetric sensors with a highly lossy resonant promoter for enhanced chromaticity. *Adv. Sci.* **7**, 2000978 (2020).
17. S. Daqiqeh Rezaei, Z. Dong, J. Y. E. Chan, J. Trisno, R. J. H. Ng, Q. Ruan, C. W. Qiu, N. A. Mortensen, J. K. W. Yang, Nanophotonic structural colors. *ACS Photonics.* **8**, 18–33 (2021).
18. H. Eoh, Y. Jung, C. Park, C. E. Lee, T. H. Park, H. S. Kang, S. Jeon, D. Y. Ryu, J. Huh, C. Park, Photonic crystal palette of binary block copolymer blends for full visible structural color encryption. *Adv. Funct. Mater.* **32**, 2103697 (2022).
19. M. Qin, M. Sun, R. Bai, Y. Mao, X. Qian, D. Sikka, Y. Zhao, H. J. Qi, Z. Suo, X. He, Bioinspired hydrogel interferometer for adaptive coloration and chemical sensing. *Adv. Mater.* **30**, 1800468 (2018).
20. S. Banisadr, A. Oyefusi, J. Chen, A versatile strategy for transparent stimuli-responsive interference coloration. *ACS Appl. Mater. Interfaces* **11**, 7415–7422 (2019).
21. S. Chen, S. Rossi, R. Shanker, G. Cincotti, S. Gamage, P. Kühne, V. Stanishev, I. Engquist, M. Berggren, J. Edberg, V. Darakchieva, M. P. Jonsson, Tunable structural color images by UV-patterned conducting polymer nanofilms on metal surfaces. *Adv. Mater.* **33**, 2102451 (2021).
22. L. Yu, H. Xu, T. M. Monro, D. G. Lancaster, Y. Xie, H. Zeng, G. Y. Chen, X. Liu, Ultrafast colorimetric humidity-sensitive polyelectrolyte coating for touchless control. *Mater. Horizons.* **4**, 72–82 (2017).
23. J. Jang, K. Kang, N. Raeis-Hosseini, A. Ismukhanova, H. Jeong, C. Jung, B. Kim, J. Lee, I. Park, J. Rho, Self-powered humidity sensor using chitosan-based plasmonic metal–hydrogel–metal filters. *Adv. Opt. Mater.* **8**, 1901932 (2020).
24. H. Kwon, S. Kim, Chemically tunable, biocompatible, and cost-effective metal–insulator–metal resonators using silk protein and ultrathin silver films. *ACS Photonics.* **2**, 1675–1680 (2015).
25. S. Arif, M. Umar, S. Kim, Interacting metal–insulator–metal resonator by nanoporous silver and silk protein nanomembranes and its water-sensing application. *ACS Omega.* **4**, 9010–9016 (2019).
26. D. Chen, T. Wang, G. Song, Y. Du, J. Lv, X. Zhang, Y. Li, L. Zhang, J. Hu, Y. Fu, R. Jordan, Dynamic tunable color display based on metal–insulator–metal resonator with polymer brush insulator layer as signal transducer. *ACS Appl. Mater. Interfaces* **11**, 41668–41675 (2019).
27. S. D. Rezaei, J. Ho, A. Naderi, M. T. Yaraki, T. Wang, Z. Dong, S. Ramakrishna, J. K. W. Yang, Tunable, cost-effective, and scalable structural colors for sensing and consumer products. *Adv. Opt. Mater.* **7**, 1900735 (2019).
28. P. Mao, C. Liu, Y. Niu, Y. Qin, F. Song, M. Han, R. E. Palmer, S. A. Maier, S. Zhang, Disorder-induced material-insensitive optical response in plasmonic nanostructures: Vibrant structural colors from noble metals. *Adv. Mater.* **33**, 2007623 (2021).
29. T. Kim, E.-S. Yu, Y.-G. Bae, J. Lee, I. S. Kim, S. Chung, S.-Y. Lee, Y.-S. Ryu, Asymmetric optical camouflage: Tuneable reflective colour accompanied by the optical Janus effect. *Light Sci. Appl.* **9**, 175 (2020).
30. D. Franklin, Z. He, P. Mastranzo Ortega, A. Safaei, P. Cencillo-Abad, S.-T. Wu, D. Chanda, Self-assembled plasmonics for angle-independent structural color displays with actively addressed black states. *Proc. Natl. Acad. Sci.* **117**, 13350–13358 (2020).
31. P. Mao, C. Liu, F. Song, M. Han, S. A. Maier, S. Zhang, Manipulating disordered plasmonic systems by external cavity with transition from broadband absorption to reconfigurable reflection. *Nat. Commun.* **11**, 1538 (2020).
32. P. Mao, C. Liu, X. Li, M. Liu, Q. Chen, M. Han, S. A. Maier, E. H. Sargent, S. Zhang, Single-step-fabricated disordered metasurfaces for enhanced light extraction from LEDs. *Light Sci. Appl.* **10**, 180 (2021).
33. A. T. Fafarman, S. H. Hong, H. Caglayan, X. Ye, B. T. Diroll, T. Paik, N. Engheta, C. B. Murray, C. R. Kagan, Chemically tailored dielectric-to-metal transition for the design of metamaterials from nanoimprinted colloidal nanocrystals. *Nano Lett.* **13**, 350–357 (2013).
34. S. J. Kim, H. K. Choi, H. Lee, S. H. Hong, Solution-processable nanocrystal-based broadband fabry-perot absorber for reflective vivid color generation. *ACS Appl. Mater. Interfaces* **11**, 7280–7287 (2019).
35. D. R. Rohindra, A. V. Nand, J. R. Khurma, Swelling properties of chitosan hydrogels. *South Pacific J. Nat. Appl. Sci.* **22**, 32–35 (2004).
36. L. H. Chen, T. Li, C. C. Chan, R. Menon, P. Balamurali, M. Shaillender, B. Neu, X. M. Ang, P. Zu, W. C. Wong, K. C. Leong, Chitosan based fiber-optic Fabry–Perot humidity sensor. *Sens. Actuators B* **169**, 167–172 (2012).
37. D. Sikdar, A. A. Kornyshev, An electro-tunable Fabry–Perot interferometer based on dual mirror-on-mirror nanoplasmonic metamaterials. *Nanophotonics.* **8**, 2279–2290 (2019).
38. H.-S. Lee, M. Q. Yee, Y. Y. Eckmann, N. J. Hickok, D. M. Eckmann, R. J. Composto, Reversible swelling of chitosan and quaternary ammonium modified chitosan brush layers: Effects of pH and counter anion size and functionality. *J. Mater. Chem.* **22**, 19605–19616 (2012).
39. D. R. Smith, D. C. Vier, T. Koschny, C. M. Soukoulis, Electromagnetic parameter retrieval from inhomogeneous metamaterials. *Phys. Rev. E Stat. Nonlinear, Soft Matter Phys.* **71**, 036617 (2005).
40. D. R. Smith, S. Schultz, P. Markoš, C. M. Soukoulis, Determination of effective permittivity and permeability of metamaterials from reflection and transmission coefficients. *Phys. Rev. B Condens. Matter Mater. Phys.* **65**, 195104 (2002).
41. L. Wang, M. S. H. Boutilier, P. R. Kidambi, D. Jang, N. G. Hadjiconstantinou, R. Karnik, Fundamental transport mechanisms, fabrication and potential applications of nanoporous atomically thin membranes. *Nat. Nanotechnol.* **12**, 509–522 (2017).
42. C. Jung, G. Kim, M. Jeong, J. Jang, Z. Dong, T. Badloe, J. K. W. Yang, J. Rho, Metasurface-driven optically variable devices. *Chem. Rev.* **121**, 13013–13050 (2021).
43. J. Li, Y. Chen, Y. Hu, H. Duan, N. Liu, Magnesium-based metasurfaces for dual-function switching between dynamic holography and dynamic color display. *ACS Nano* **14**, 7892–7898 (2020).
44. J. Li, S. Kamin, G. Zheng, F. Neubrech, S. Zhang, N. Liu, Addressable metasurfaces for dynamic holography and optical information encryption. *Sci. Adv.* **4**, eaar6768 (2018).
45. Z. Wang, C. Dai, J. Zhang, D. Wang, Y. Shi, X. Wang, G. Zheng, X. Zhang, Z. Li, Real-time tunable nanoprinting-multiplexing with simultaneous meta-holography displays by stepwise nanocavities. *Adv. Funct. Mater.* **2021**, 2110022 (2021).
46. S. S. Voznesenskiy, A. A. Sergeev, A. Y. Mironenko, S. Y. Bratskaya, Y. N. Kulchin, Integrated-optical sensors based on chitosan waveguide films for relative humidity measurements. *Sens. Actuators B* **188**, 482–487 (2013).


**Acknowledgments:** We thank J. Park (POSTECH) for the technical support in simulation. **Funding:** This work was financially supported by a Samsung Research Funding and Incubation Center for Future Technology grant (SRFC-IT1901-05) funded by Samsung Electronics. S.-J.K. acknowledges an ETRI internal grant (21ZB1130). J.J. acknowledges a Hyundai Motor Chung Mong-Koo fellowship. **Author contributions:** Conceptualization: C.J., S.-J.K., J.J., and J.R. Fabrication: C.J., S.-J.K., and B.K. Simulation: C.J. and J.J. Measurement: C.J., S.-J.K., J.H.K., and D.K. Supervision: Y.M.S., S.-H.H., and J.R. Writing—original draft: C.J., S.-J.K., and J.J. Writing—review/revision: J.R. **Competing interests:** The authors declare that they have no competing interests. **Data and materials availability:** All data needed to evaluate the conclusions in the paper are present in the paper and/or the Supplementary Materials.

Submitted 17 October 2021
Accepted 21 January 2022
Published 11 March 2022
10.1126/sciadv.abm8598